

Ultrafast enhancement of electron-phonon coupling via dynamic quantum well states

Samuel T. Ciocys^{1,2} & Alessandra Lanzara^{1,2}  ^{1,2}✉

The density of states at the Fermi surface controls many material properties by influencing the low-energy interactions of conductive electrons. Typically, external tuning knobs generate only small perturbations to the density of states in crystals, since their band structure depends strongly on the lattice potential. In contrast, quantum well states are contingent on a localized potential extrinsic to the crystal lattice and can be easily modified leading to changes in the density of states at the Fermi level. Here, we are able to control the quantum well potential on the surface of Bi_2Se_3 with light, driving a density of states singularity below E_F at ultrafast timescales, thereby triggering a reversible Lifshitz transition. We reveal a substantial ultrafast enhancement of the electron-phonon coupling with repercussions on the relaxation dynamics in the system. We argue that the relaxation dynamics are governed largely by the interplay of the dynamic density of states of the quantum wells with c -axis scattering from the A_{1g}^2 optical phonon mode. These results demonstrate a powerful way to enhance electron-boson interaction on ultrafast timescales providing new avenues for controlling material properties and driving novel quantum phases of matter.

¹Department of Physics, University of California, Berkeley, CA 94720, USA. ²Materials Science Division, Lawrence Berkeley National Laboratory, Berkeley, CA 94720, USA. ✉email: alanzara@lbl.gov

Electron-phonon coupling (EPC) is among the most fundamental interactions in solids, adding to the complexity of electronic behavior beyond the Coulomb interaction. Not only does EPC play an important role in defining the electronic, transport, optical and thermal properties of materials, but it is also fundamental in driving novel quantum phases of matter, such as superconductivity, charge density waves, and 2D Ising materials^{1–5}.

Since EPC is strongly dependent on the density of states (DOS) at the chemical potential^{3,6,7}, various methods have been developed to tune the chemical potential in a controlled way and induce changes in the coupling constant. These changes can be particularly relevant in the presence of singularities in the DOS, as is generally the case in the proximity of a Lifshitz transition^{8–11}, where very large enhancements of the coupling constant can be realized by placing the chemical potential at the singularity. Most of the methods adopted so far rely on tuning of static parameters such as temperature, doping, pressure and electrostatic gating^{12–15}, with the latter being the most versatile as it does not modify the underlying lattice. 2D quantum well (QW) states, are ideal candidates to controlling Lifshitz transitions, due to their malleable quantized band structure, which in the presence of the Rashba Effect leads to singularities in the DOS^{16,17}.

The recent discovery that light can be used to modulate the underlying potential in QWs and to induce a Lifshitz transition¹⁸, opens up the intriguing possibility to tune EPC on ultrafast time scales through DOS alone, and present a new avenue for engineering boson-mediated quantum phases. Time and angle resolved photoemission spectroscopy (TR-ARPES) is ideal to study these effects as it allows a direct measurements of the underlying modification of the band structure and of the electron-phonon coupling constant^{19,20}.

In this study, we utilize TR-ARPES to drive a Lifshitz transition of a van-Hove-like singularity in the surface quantum wells of Bi₂Se₃. As the singularity returns to the Fermi level, we reveal a transient enhancement of the EPC that affects the electron-hole recombination process and abruptly transfers charge to the surface. Based on experimental indications of *c*-axis scattering and a characteristic phonon energy from the electronic self-energy in the topological surface, we describe a direct phonon emission model for relaxation involving the A_{1g}² optical phonon mode that closely captures the relaxation dynamics. Altogether, this work establishes a simple means of controlling large changes in the DOS at the Fermi level and enhancement of the electron-boson interaction on ultrafast timescales by harnessing the flexible spectrum of quantum well states.

Results

A transiting singularity. Figure 1a, b present an overall summary of the ultrafast photo-induced Lifshitz transition in the QW spectrum. The infrared pulse generates excited electrons and holes that cancels the surface band bending. Panel (a) shows the typical spectra of Rashba-split quantum well states before and after infrared illumination. At equilibrium (panel (a)) only the first quantum well (QW1) is filled, with the two spin-split bands resolved. The corresponding band bottom defines a ring of non-zero radius, in contrast to point-like as in the case of spin degenerate band. Consequently, the DOS is no longer a step function, but increases asymptotically in correspondence to the band bottom, akin to a van-Hove singularity¹⁶ (see leftmost panel).

Upon illumination, the surface photovoltage effect is known to modify the potential gradient of the quantum well¹⁸, producing a transient shift of the QW energies that can drive QW2 below the Fermi level (panel (b)). An infrared pulse generates electron-hole

pairs at the surface of the sample with strong downward band-bending. The electrons are pushed towards the surface by the downward band bending field while holes are pushed into the bulk. The subsequent transient dipole field created by the separated photoexcited charges reduces the equilibrium band bending field, thereby altering the quantum well potential at the surface. Subsequently, QW1 and QW2 shift downward and photoexcited charge is stored in the shifted high energy portion of the QW1 dispersion and the singularity in QW2. Accordingly, within this picture, our pump-probe experiment is toggling the DOS singularity of QW2 below and then back above the Fermi level. The downward shifting of QW1 does not affect the Fermi surface topology, but the emergence of QW2 below the Fermi level introduces two new electron pockets, producing a time-dependent Lifshitz transition. This ability to reversibly and continuously control the position of the van Hove singularity with respect to E_F presents an ideal condition for enhancing electron-phonon interaction.

Additionally, since the photogenerated dipole changes the surface potential, the kinetic energies of the photoemitted electrons are rigidly shifted accordingly. This rigid shift is removed in the resulting ARPES spectra throughout this study to reveal the underlying electron dynamics^{21,22} (see Supplementary Fig. 1).

Figure 1c displays the raw ARPES spectra of the Bi₂Se₃ surface QW states at equilibrium as well as at five representative delays ($\tau = 10, 60, 120, 180, 370$ ps) pumped at $51.9 \mu\text{J} \cdot \text{cm}^{-2}$. At equilibrium, the TSS and the lowest energy quantum well dispersion (QW1) are present and filled below E_F , with QW1 demonstrating strong Rashba splitting. After pump excitation ($\tau = 10$ ps), the second Rashba-split quantum well dispersion (QW2) appears below E_F and is subsequently filled via thermal relaxation. At more positive delays, QW1 and QW2 relax towards their equilibrium energies. In particular, $\tau = 120$ ps represents an important moment in the quantum well relaxation, corresponding to the time when the QW2 band bottom and DOS singularity reach the Fermi level. We will refer to this time as τ_{cross} .

The delay time τ_{cross} corresponds to two peculiar phenomena in the delay-dependent spectra represented in panels (d) and (e), respectively: 1) a discontinuity in the decay rate of photoexcited charge, top panel (d). 2) a rapid broadening of the TSS and quantum well dispersions in panel (e). In the top subpanel of Fig. 1d, we present the total spectral intensity of QW1 and QW2 as a function of delay over the fluence range $2.9 - 59.1 \mu\text{J} \cdot \text{cm}^{-2}$ using the dashed white integration window shown for $\tau = 370$ ps in panel (c). At high fluence, charge is stored below E_F and decays slowly up until τ_{cross} (dashed line serves as visual guide), where charge begins to decay rapidly.

The crossing of the QW2 band bottom back above the Fermi level is clearly observed in the time-dependent states at the Fermi level (vertical dashed line) displayed in the TR-ARPES map in the bottom subpanel of Fig. 1d. Here, QW1 states that cross E_F can be seen as continuous lines as a function of delay near $k_x \approx \pm 0.1$ and $\pm 0.06 \text{ \AA}^{-1}$, experiencing slight inward bending as the QW spectrum relaxes. Whereas QW2 states appears at $k_x \approx \pm 0.045 \text{ \AA}^{-1}$ and approach $k_x = 0$ as the band bottom crosses the Fermi level at delay $\tau \approx 120$ ps, marking the reversal of the pump-induced Lifshitz transition.

The second effect of rapid spectral broadening is best observed in Fig. 1e. The comparison between $\tau = 10$ ps and $\tau = 120$ ps of the surface bands including QW1, QW2, and the TSS reveals a significant increase in spectral broadening at τ_{cross} . The bottom panel displays the momentum distribution curves (MDCs) at 50 meV below the Fermi level demonstrating that the spectral linewidth in the momentum direction increases for both the TSS and QW1.

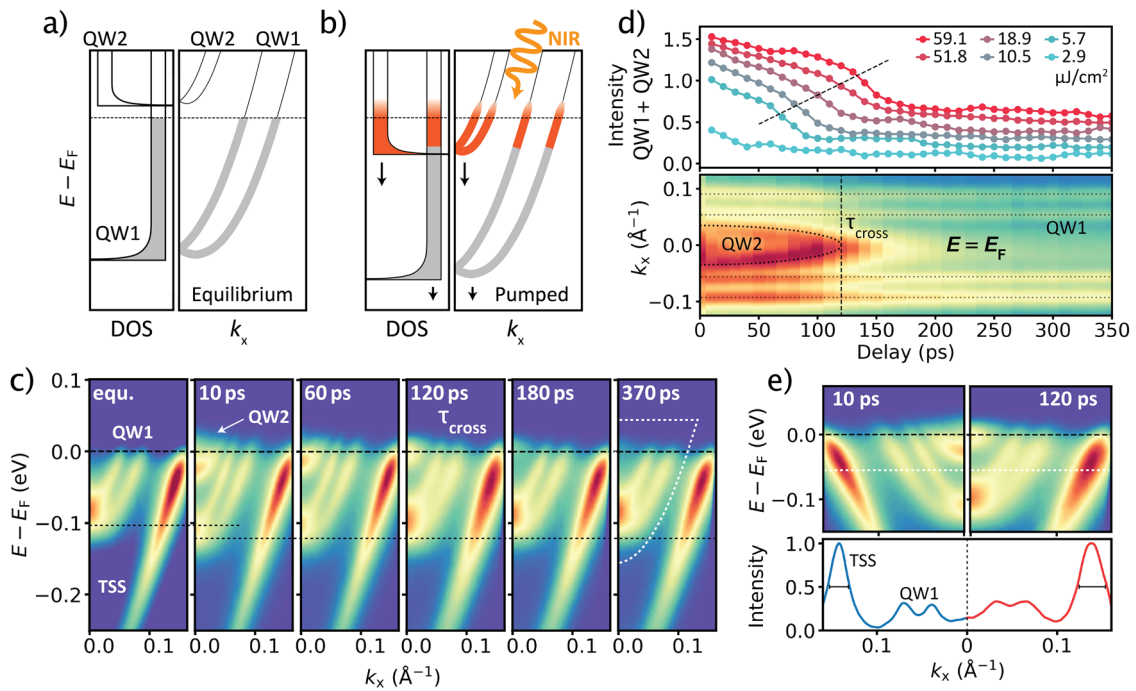


Fig. 1 Controlling Rashba singularity with an ultrafast Lifshitz transition. **a** Schematic of light induced Lifshitz transition and DOS singularities. Before the pump, QW2 is above E_F and unoccupied. **b** After illumination, QW1 and QW2 shift downwards, QW2 is filled, and the Fermi surface acquires higher order topology. **c** Spectra at equilibrium, 10 ps, and 350 ps showing the emergence of QW2 below E_F and subsequent return above E_F at τ_{cross} . **d** Top: Integrated spectral intensity of full QW1 and QW2 dispersions (dashed white region (**b**) at $\tau = 370$ ps) over all measured fluences. At fluences $> 4 \mu\text{J} \cdot \text{cm}^{-2}$, charge decay experiences a transition from a long-timescale process to rapid recombination at τ_{cross} (dashed black line guide to the eye). Bottom: TR-ARPES map at E_F demonstrating the crossing of the QW2 band bottom (dashed black line). **e** Broadening of dispersions at τ_{cross} . MDCs at $E = -0.50$ eV show increased linewidths at τ_{cross} versus 10 ps. Panels (**c**), bottom (**d**), and (**e**) are for fluence $51.8 \mu\text{J} \cdot \text{cm}^{-2}$.

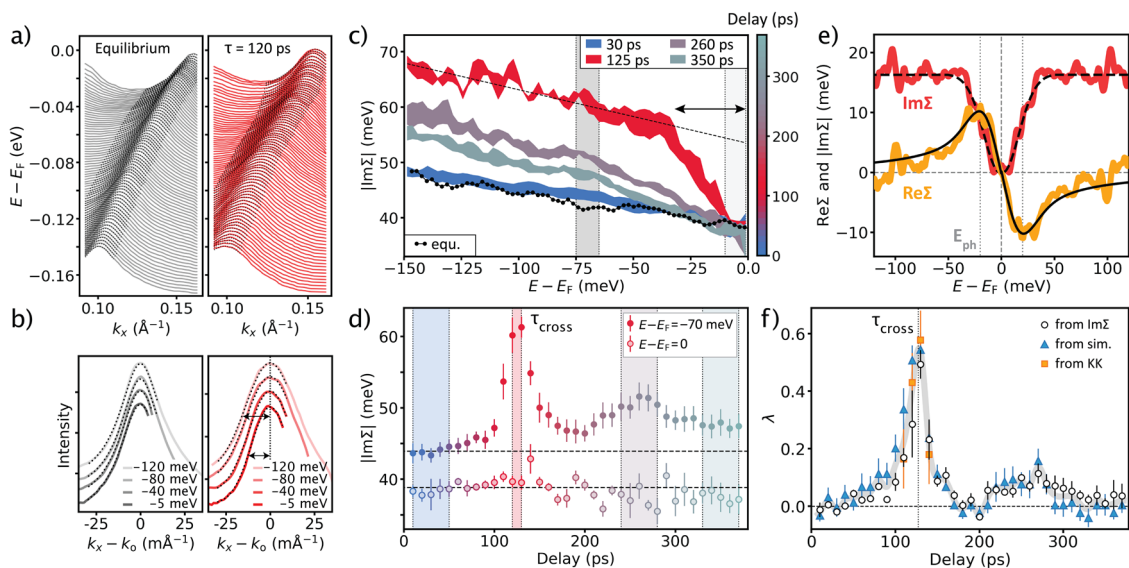


Fig. 2 Ultrafast transient self-energy enhancement. **a** MDCs of TSS at equilibrium and 120 ps demonstrating transient broadening and goodness of Lorentzian fits. **b** MDCs of TSS at four binding energies with centroids aligned showcasing the increased broadening at 120 ps (red) versus equilibrium (grey) particularly for high binding energies (see arrows). **c** $\text{Im}\Sigma$ derived from MDC Lorentzian FWHM as a function of binding energy at equilibrium and four representative delay integration windows (corresponding shaded regions in **d**). $\text{Im}\Sigma$ as a function delay from dark grey energy window shown in **d** (dark circles) and light grey energy window shown in **d** (light circles). **e** $\text{Im}\Sigma$ at 120 ps (red) with linear component removed and corresponding $\text{Re}\Sigma$ from Kramers-Kronig transform (yellow). Dashed and solid black lines correspond to $\text{Im}\Sigma$ and $\text{Re}\Sigma$ from simulating 120 ps spectrum. **f** The electron-phonon coupling constant, λ , determined from high binding energy plateau of $\text{Im}\Sigma$ of **c** (white circles), optimizing MDC centroid locations through spectra simulations (blue triangles), and Kramers-Kronig of measured $\text{Im}\Sigma$ of **e** (yellow squares).

Self-energy implications of rapid spectral broadening at τ_{cross} . To better understand the impact of this photo-induced transition on many body interactions, in Fig. 2 we study its effect on the real and imaginary part of the electron self-energy ($\text{Re}\Sigma$ and $\text{Im}\Sigma$), quantities that can be directly accessed by ARPES, which measures the single particle spectral function:

$$A(k, \omega) = \frac{1}{\pi} \frac{|\text{Im}\Sigma(k, \omega)|}{(\omega - E_0(k) - \text{Re}\Sigma(k, \omega))^2 + \text{Im}\Sigma(k, \omega)^2} \quad (1)$$

where k and ω are the electron momentum and energy, respectively, $E_0(k)$ is the energy of the bare band, and $\text{Re}\Sigma(k, \omega)$ and $\text{Im}\Sigma(k, \omega)$ are the real and imaginary parts of the electron self-energy. $\text{Re}\Sigma(k, \omega)$ and $\text{Im}\Sigma(k, \omega)$ are Kramers-Kronig related and are shaped by many-body interactions. The imaginary part of the self-energy broadens the energy distribution curve (EDC) linewidth whereas the real part modifies the bare band dispersion location. The linewidth and band dispersion can be extracted by either EDCs or MDCs.^{19,20}

As shown in Equation (1), the ARPES spectral function takes the form of a Lorentzian with the full-width-at-half-maximum (FWHM) in the energy direction, Γ_ω , equal to $2|\text{Im}\Sigma(k, \omega)$. Therefore, EDCs provide a direct measure of the $\text{Im}\Sigma(k, \omega)$. Similarly, the self-energy can be extracted from the FWHM in the momentum direction for a near-linear dispersion via $|\text{Im}\Sigma(k, \omega)| = \Gamma_k v_F/2$. The latter method using MDCs is more precise as it avoids asymmetric effects from the Fermi Dirac distribution^{19,20}.

Figure 2a shows the MDCs at equilibrium (grey) and 120 ps (red) with Lorentzian fits (black dashed). The comparison of the raw spectra reveals a dramatic increase of the MDC width at $\tau_{\text{cross}} = 120$ ps over a large binding energy range. Figure 2b presents a closer inspection of the MDCs and fits for four evenly spaced binding energies. Particularly at 120 ps, the MDCs dramatically reduce in linewidth as the binding energy approaches E_F (see arrows) (see Supplementary Fig. 2 for more details).

Figure 2c plots $\text{Im}\Sigma$ (extracted from MDCs in the red window of panel (a) versus binding energy at equilibrium (black dots) and four integrated delay regions (see corresponding shaded colors in panel (d)) denoted by the average delay value. At equilibrium and 10 ps, $\text{Im}\Sigma$ is approximately flat and at a minimum. At τ_{cross} and above -30 meV, the self-energy trends sharply downward towards the equilibrium value at E_F . At longer delays (170 ps and 350 ps) the self-energy remains above the equilibrium position at high binding energies with a downward slope towards the equilibrium value at E_F .

The energy-dependence of the imaginary part of the self-energy at τ_{cross} in panel (c) is emblematic for electron-phonon coupling, where $\text{Im}\Sigma$ demonstrates a step-like function that is large for energies below the phonon-mode energy, E_{ph} , and decreases towards E_F for energies above E_{ph} , manifesting in a characteristic dip in self-energy between E_{ph} and E_F (see horizontal arrows and red curve)^{3,19,20,23}. In this specific case, the energy of the self-energy dip is consistent with a previously observed phonon mode of $E_{\text{ph}} \approx 20$ meV known to couple to both the bulk and surface states at varying degrees^{20,24,25}. This phonon mode has been associated with the optically active A_{1g}^2 mode^{20,25–28}. The dip near E_F is suppressed for all other delays, suggesting that EPC from the 20 meV phonon increases at the moment of τ_{cross} . The constant offset for all delays of ≈ 40 meV ($\text{Im}\Sigma$ value at $E - E_F = 0$) is indicative of the electron-disorder interaction and is delay-independent and comparable to previous reports in Bi_2Se_3 ^{20,29,30}. Furthermore, overall there is delay-dependent linear component of $\text{Im}\Sigma$ (dashed line) that could indicate weak electron-electron coupling, $\beta \approx 0.0005$, consistent

with previous equilibrium studies of Bi_2Se_3 ^{20,30} or a previously reported unknown final-state effect¹⁹.

The evolution of the $\text{Im}\Sigma$ as a function of delay time is shown in Fig. 2d. Spectra are shown both at high binding energy represented by dark circles (from dark grey integration window in panel (c)) and at E_F represented by lightened circles (from light grey integration window in panel (c)). The primary feature of the $\text{Im}\Sigma$ profile at high binding energy is a sharp peak that occurs at τ_{cross} . Moreover, $\text{Im}\Sigma$ remains raised above the equilibrium value (black dashed) for positive delays beyond the τ_{cross} . However, $\text{Im}\Sigma$ near E_F which serves as a measure of the degree of electron-disorder interaction, is delay independent and consistent with previous reports in Bi_2Se_3 ^{20,29,30}.

Additionally, we have performed a bottom-up simulation of the ARPES spectrum with the effect of EPC under the influence of energy and momentum broadening (see Supplementary Fig. 4). The inherent broadening from the detector obscures direct measurement of the real-part of the self-energy from panel (a). Simulated spectra are generated by varying $\text{Re}\Sigma$ and the corresponding Kramers-Kronig consistent $\text{Im}\Sigma$ of a 20 meV phonon mode applied to the bare band dispersion with the electron-phonon coupling constant, λ , as the variable parameter. Within this method, we have assumed that λ is near-zero at equilibrium based on similarly doped equilibrium systems from literature^{20,31}. This assumption is consistent with the extrapolated bare band in Supplementary Fig. 3, which (although it experiences positive curvature) does not demonstrate a kink near 20 meV. We can then determine a resulting $\text{Re}\Sigma$ and $\text{Im}\Sigma$ that minimize the difference between MDC centroid locations between the simulated and experimental data, circumventing the detector resolution effects. The results from panel (c) are consistent with the simulated spectra, as can be seen in Fig. 2e. From the measured $\text{Im}\Sigma$ in panel (c) we can determine $\text{Re}\Sigma$ through the Kramers-Kronig transformation and compare both self-energy components to the best fit self-energies determined from the bottom-up spectra simulations. Panel (e) then presents $\text{Im}\Sigma$ (red) for 120 ps after removing the linear background (dashed line in panel (c)) and $\text{Re}\Sigma$ (yellow) as determined through Kramers-Kronig analysis with the respective self-energies from the simulation overlaid in dashed and solid black, respectively. The Kramers-Kronig analysis reveals a $\text{Re}\Sigma$ peaked at 20 meV near the expected E_{ph} . Both experimental self-energy components closely match the respective self-energies from the simulation.

The results discussed so far suggest an increase of $\text{Im}\Sigma$ at the characteristic phonon frequency and consequent renormalization of the dispersion indicative of electron-phonon coupling. The strength of this coupling is defined by the electron-phonon coupling constant, λ , and can be directly extracted from the self-energy following standard procedure. Specifically, we have adopted three different methods to determine λ and study its evolution as a function of delay time. The results are consistent with each other, as shown in Fig. 2f. The three methods are described below:

1. From the measured $\text{Im}\Sigma$ in panel (c), λ is determined from the high binding energy plateau after removing the electron-disorder component (constant offset at $E - E_F = 0$) and the linear background (dashed line), which leads to the red curve in panel (e). The magnitude of λ is determined by the height of the self-energy plateau and the phonon-mode energy being $\lambda = 2|\text{Im}\Sigma(E < E_{\text{ph}})|/(\pi E_{\text{ph}})$ ^{2,32} as shown by white circles.
2. We use λ from the best fit simulation described in Supplementary Fig. 4, displayed as blue triangles.
3. By performing the Kramers-Kronig transform on the background subtracted $\text{Im}\Sigma$ (as shown in panel (e)) we

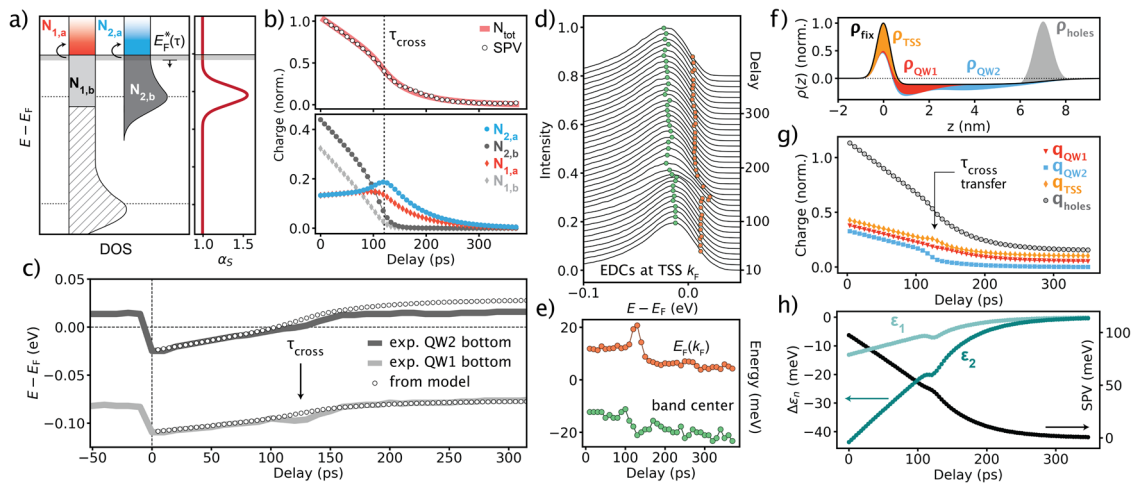


Fig. 3 Singularity-mediated relaxation dynamics. **a** DOS of QW1 and QW2 (temp. broadened) illustrating rate equation model. Model chooses energy frame in which QW2 band bottom energy is fixed. E_F^* drifts downward according to total stored charge, while charge $N_{1,b}$ and $N_{2,b}$ are transferred to $N_{1,a}$ and $N_{2,a}$ and allowed to decay with recombination rate $\alpha \cdot \alpha_s$. **b** Results of model showing good agreement with surface voltage time-dependence. **c** QW1 and QW2 band bottoms from model (light grey and dark grey, respectively) compared to measured EDC centroid band bottom locations at Γ as a function of delay (open circles). **d** EDCs at TSS k_F as a function of delay with quasi- E_F (orange) and band centers (green), demonstrating short-lived charge accumulation. **e** E_F and band centers plotted vs delay show peak occurs at τ_{cross} . **f** Charge density versus distance into the bulk used in charge transfer model. ρ_{fix} (black line) is fixed charge that creates band bending potential at equilibrium. Photoexcited electrons ρ_{TSS} , ρ_{QW1} , and ρ_{QW2} (yellow, red, blue respectively) and photoexcited holes ρ_{holes} alter the charge distribution after excitation and decay in time. **g** Decay profile of TSS, QW1, QW2, and trapped hole populations, showing charge transfer from QW2 to QW1 and TSS. **h** Charge transfer causes a dip in the relaxation of the QW1 and QW2 eigenvalues (light and dark teal, respectively) at τ_{cross} , capturing panel c behavior. Surface potential response (black) is mostly unaffected by charge transfer.

determine lambda from the slope of $\text{Re}\Sigma$ near E_F ^{2,3,20}. These results are presented as yellow squares for the four delays near τ_{cross} that exhibit a clear dip in $\text{Im}\Sigma$ and therefore a distinguishable $\text{Re}\Sigma$.

These observations suggest that the TSS undergoes a sudden increase of the electron-phonon coupling at τ_{cross} reaching a coupling constant of nearly $\lambda = 0.6$, much higher than previously reported in equilibrium studies of Bi_2Se_3 ^{20,27,31,33}. Both the TSS and bulk conduction band (of which the QWs are derived) participate in the EPC, with previous studies suggesting that the QWs in Bi_2Se_3 are a significant factor in determining EPC strength^{25,34,35}.

c-axis scattering in relaxation and charge transfer dynamics.

The Lifshitz transition and the associated self-energy enhancement play a critical role in the recombination of the photoexcited electron-hole pairs. To elucidate their role, we have developed a minimal rate-equation model that incorporates the DOS of QW1 and QW2 as well as enhanced scattering at the moment of the Lifshitz transition. At the surface of the material the conduction band and valence bands bend downwards forming a band bending potential that generates the quantum well levels. The downward band bending forces holes into the bulk and electrons towards the surface, trapping both populations and generating a separated charge distribution that manifests as (and is proportional to) the measured potential at the surface. Therefore, the decay profile of this surface potential measures the time-dependence of the photoexcited charge at the surface and it can be directly measured as a function of delay by the delay-dependent rigid shift of the ARPES spectrum according to our previous studies^{21,22}. Since the majority of photoexcited charge at the surface is trapped in the modified quantum well levels, understanding the decay mechanisms of the trapped charge in QW1 and QW2 can reveal the origin of the discontinuous decay profile of the surface potential.

Figure 3a illustrates the electronic filling of QW1 and QW2 after excitation. The equilibrium electron filling is designated by the striped regions whereas the filled regions indicate the excess electron populations created by the pump. For the non-equilibrium charge trapped in the quantum well levels, there are two types of populations: electrons above E_F : 1) both QW1 and QW2 shift downwards in energy with respect to the Fermi level and establish charge below E_F ($N_{1,b}$ and $N_{2,b}$ respectively) which remains in quasi-equilibrium (no recombination) during their stay below E_F . 2) photoexcited charges will also populate states in QW1 and QW2 above E_F ($N_{1,a}$ and $N_{2,a}$), which can recombine with bulk holes at the rate α_{rec} .

These populations are not static, since QW1 and QW2 relax upward in energy changing the relative position of E_F with respect to the band bottoms. Our model incorporates this effect by fixing the energy positions of QW1 and QW2 such that E_F in this energy frame is time dependent, $E_F^*(\tau)$. In fact, E_F^* depends proportionally on the total accumulated charge, $N_{\text{tot}} = N_{1,a} + N_{1,b} + N_{2,a} + N_{2,b}$, since the electric field linearly modifies the quantum well level positions and is proportional to the total charge.

As E_F^* shifts downward, charge from $N_{x,b}$ is transferred to $N_{x,a}$ according to the respective DOS and ΔE_F^* . The DOS of the QWs is broadened by 6 meV, the expected smearing of the DOS at $T = 80$ K³⁶. Finally, we simulate the effect of the sudden increase in λ discussed in Fig. 2 through the coefficient α_s which tracks with QW2; minimum value of 1 and a 6 meV broad Gaussian peak of +0.5 centered at the QW2 singularity. This has the effect of enhancing the recombination rate, $\alpha_{\text{rec}} = \alpha_s(E_F^*) \cdot \alpha_o$, for $N_{x,a}$ the moment E_F^* crosses the QW2 singularity as would be expected in the case of increased electron-phonon scattering^{3,37}.

Figure 3b plots the results of the model alongside the normalized surface potential profile at $51.9 \mu\text{J} \cdot \text{cm}^{-2}$, capturing both the slow decay region before τ_{cross} (vertical dashed line) as well as the kink towards exponential-like decay. The individual charge populations are shown in the bottom graph. Notably, the charge stored above E_F in QW1 and QW2 is sustained up until

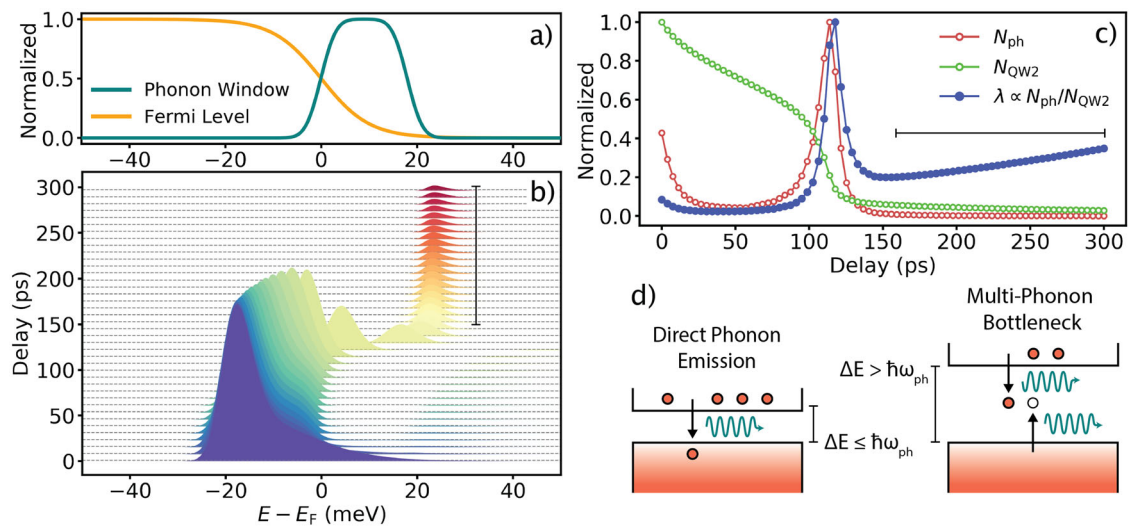


Fig. 4 Phonon dominated scattering from QW2. **a** Fermi level (orange) and single phonon relaxation window for charge above E_F (teal) used in calculation. **b** Evolution of QW2 DOS as a function of delay taking into account recombination into the bulk from A_{1g}^2 phonon mode (phonon window). The QW2 DOS shifts upward in energy at a rate proportional to ΔN_{QW2} at each time step, simulating SPV relaxation. **c** Total charge in QW2 (green), generated phonons from scattering within phonon window (red), and the effect on electron-phonon coupling (blue) as a function of delay. Charge in QW2 serves to screen electron-phonon interaction, while generated phonons enhance the coupling. **d** Illustration of phonon bottleneck effect in recombination freeze-out from QW2 spectral drift (see regions highlighted in **b**, **c**). When QW2 band bottom is less than $\hbar\omega_{ph}$, electrons can relax directly through A_{1g}^2 phonon emission. As QW2 shifts upwards in energy, a multi-phonon process is required or photon-radiative decay is required, freezing out the phonon contribution to relaxation.

τ_{cross} in which $N_{2,a}$ exhibits a hump then decay, and $N_{1,a}$ transitions into exponential-like decay (see Supplementary Figs. 5–7 for details on the model).

Figure 3c displays measured band bottom energy positions of QW1 and QW2 (light grey and dark grey respectively) as a function of delay determined from the EDC peak positions at Γ . Since E_F^* measures the relative distance between the QW2 band bottom and E_F , we can extrapolate the QW1 and QW2 band bottom positions from our model (open circles) by monitoring E_F^* versus delay. The model-extrapolated QW2 band bottoms using the same parameters in panel (b) match the measured QW2 band bottom position up until QW2 crosses E_F . At this point, the EDC peak positions for QW2 no longer capture the true band bottom positions due to convolution with the Fermi level. However, we can see agreement of the model for further delays by investigating the measured QW1 band bottom position which is unaffected by the Fermi level. The open circles plotted beneath QW2 represents $E_F^*/1.65$, offset to match the QW1 energy position at $\tau = 0$ ps and divided by 1.65 (the empirically determined proportionality constant between QW1 and QW2 energy levels, see Supplementary Fig. 8). As verification, we see that the experimentally determined QW1 band bottom positions match the simulation closely across the entire delay range.

However, if one looks closely at panel (c), QW1 appears to dip momentarily in energy at τ_{cross} (see arrow). Figure 3d–h presents a reasonable explanation for this phenomenon that again takes into account increased scattering during the Lifshitz transition.

From our earlier discussion of Fig. 3, it is clear that the EPC enhancement is associated with an increase in c -axis scattering causing an increase in the electron-hole recombination rate. However, it is likely that this scattering is not unidirectional towards the bulk and due to the intrinsic downward bending in the material, electrons are already pressured towards the surface^{22,38}. In the low-scattering regime before τ_{cross} few electrons participate in indirect scattering to the TSS. However, at τ_{cross} the scattering rate increases driving charge both into the

bulk and towards the surface and momentarily producing an excess of charge in TSS.

In fact, this behavior is observed at k_F of the TSS. In Fig. 3d we present EDCs at k_F that are offset according to their corresponding delay time. The Lorentzian band centers (green) and the quasi-Fermi-level (orange) demonstrate opposing hump-like behavior at τ_{cross} . This can be seen more clearly in Fig. 3e in which only the band centers and $E_F(k_F)$ are plotted versus delay. The sharp increase in the quasi-Fermi-level at τ_{cross} suggests that charge is transferred to the TSS and exists over a short timescale (< 20 ps).

In light of the observed excess charge in the TSS at τ_{cross} , we explore the consequences of such a charge transfer using a partially coupled Poisson-Schrödinger method to simulate charge populations and calculate QW wave-functions (see Supplementary Fig. 9). In Fig. 3f, we plot the relevant charge densities at the surface and in the bulk used in our model. The equilibrium fixed charge distribution, ρ_{fix} , is shown as the black curve and established the equilibrium band bending potential. After the pump pulse, photoexcited charge separation leads to excess electron populations ρ_{TSS} , ρ_{QW1} , and ρ_{QW2} (yellow, red, and blue, respectively) and an equal number of holes at the bulk edge of the band bending, ρ_{holes} (grey). The charge in QW1 and QW2 is determined by the square modulus of the resulting wave-functions confined in the non-equilibrium band bending potential.

The excited charge populations decay according to a simulated surface potential decay profile shown in panel (g). The simulated surface potential decay profile can be seen in the excited hole population, q_{holes} , which is equal to the summation of the excited QW1, QW2, and TSS populations, maintaining charge neutrality. In order to simulate the charge transfer towards the surface, we introduce a sigmoidal reduction in the charge population of QW2 that is transferred to q_{TSS} and q_{QW1} asymmetrically, with a Gaussian excess at τ_{cross} given to q_{TSS} and the remainder provided to q_{QW1} . This produces the effect of a biased charge transfer to the

TSS (see arrow) which is then equilibrated with QW1 after τ_{cross} . The curves have been shifted vertically slightly for visibility.

The non-equilibrium charge distribution in panel (f) is thus determined from recursively adding charge to the equilibrium band bending based on the charge decay profiles in panel (g), altering the potential based on Poisson's equation, calculating the new charge distribution from the wavefunctions from Schrödinger's equation, and producing a new band bending potential in small steps. The reverse order of the results produces the time-dependent wave function dynamics. Figure 3h plots the change in eigenvalues of QW1 (light teal) and QW2 (dark teal) as a function of delay, demonstrating the dipped feature observed in panel (c). The model underestimates the shift of QW1 by a factor of two, but closely captures the shape of the time dependence. The surface voltage can be determined in our simulation by the difference in bulk and surface potentials (black) and is only weakly affected by the charge transfer event. This is expected since the change in surface potential is mainly determined by the total population of photoexcited electrons and holes.

Scattering enhancement and recombination freeze-out via phonon bottleneck mechanism. We have shown in Fig. 2 that the time-dependence of the self-energy of the TSS indicates an enhancement of the electron-phonon coupling at τ_{cross} . Then in Fig. 3 we have demonstrated that recombination driven by the cross-section of the time-dependent DOS of the dynamic QW2 spectrum with an energy-dependent scattering rate (α_s) phenomenologically captures the experimentally measured stored-charge profile as determined from the SPV decay (Fig. 3b) and the time-dependence of the QW energy levels (Fig. 3c). Moreover, we confirm that *c*-axis scattering is indeed playing a large role in the recombination process at τ_{cross} by evidence of the abrupt jumps in the QW energy levels as QW2 crosses E_F (Fig. 3c, h). The remaining question is what generates the energy dependent scattering rate, α_s , driving the complex recombination process?

In Fig. 4, we present a model that captures the scattering enhancement at τ_{cross} by means of direct recombination through phonon emission. The primary assumption is the that direct recombination through photon-radiative recombination is greatly inhibited by the spatial separation of the photoexcited charge by the band bending potential. This means that recombination is primarily driven by phonons that scatter along the *c*-axis, making the A_{1g}^2 optical phonon mode a prime candidate for such a mediator^{26,28,39,40}. The teal curve in Fig. 4a approximates the window for which electrons above E_F can recombine with holes at E_F given a single phonon emission with energy ω_{ph} . For electrons with energies above ω_{ph} , recombination through *c*-axis scattering requires either a two phonon process and therefore greatly reduced scattering probabilities, or single phonon plus single photon radiative decay, again a less probable decay channel. The general concept is depicted in Fig. 4d where direct phonon relaxation is determined by the gap between the conduction band bottom (upper region) and the top of the valence band (red filled lower region). When the gap is greater than ω_{ph} , recombination is reduced, a process often referred to as a phonon bottleneck^{41,42}.

Figure 4b shows the time-dependence of the QW2 DOS (singularity included) with the initial state multiplied by the Fermi distribution in panel (a) and broadened by 10 meV. At each time step charge relaxes proportional to the energy-dependent phonon window, and the DOS shifts upward in energy at a rate proportional to the change in the integrated DOS (ΔN_{QW2}), similar to the model in Fig. 3 but ignoring contributions from QW1 for simplicity. At delays past $\tau_{\text{cross}} = 120$ ps (vertical bar), the QW2 DOS is greatly diminished and at the edge

of the phonon window, prolonging the lifetime of excited charge above E_F .

Panel (c) displays the time-dependence of the charge in QW2 (green) and the generated phonons due to recombination (red). The electron-phonon coupling is dependent on both of these parameters. The electrons stored at the surface act to screen lattice vibrations such that electron-phonon coupling is inversely proportional to excess charge carriers, and EPC is directly proportional to the number of available phonons for scattering, so that together $\lambda \propto N_{\text{ph}}/N_{\text{QW2}}$ ^{43–45}. By including a small constant background for N_{ph} (0.10% of peak) to accommodate possible higher order sources of phonons, then the blue points in panel (c) depicts the time-dependence of the EPC constant. The spike in generated phonons at τ_{cross} would result in a corresponding electron heating event, and this is indeed observed in the Fermi level broadening of QW1 and TSS (see Supplementary Fig. 10). Notice that for delays beyond τ_{cross} (horizontal bar), the electron coupling constant remains elevated due to the non-zero phonon background, and even increases gradually due to the slow decay of the QW2 DOS. This effect could explain the increased imaginary self-energy for delays between 200 and 300 ps that leads to a similar bump in the calculated electron-phonon constant (see Fig. 2d, f).

Discussion

In this study, we have uncovered sub-resolution effects (namely the 20 meV phonon kink) by simulating the effect of a kinked dispersion on the MDC centroids. TR-ARPES suffers from intrinsically poor energy resolution in part due to the Fourier limitation of the bandwidth of the sub-picosecond pulses. The time-resolution can in principle be reduced to improve the energy resolution, however this limits the ability to study typical electronic lifetimes⁴⁶. We have shown in this study that the prior knowledge of the location and functional effect of the phonon modification to the bare band is sufficient to peer beneath the intrinsic broadening. Although, there have been numerous studies on the effect of detector broadening on MDC and EDC fits to dispersions^{23,47–49}, this study is original in the sense that we have focused on non-equilibrium near- E_F modifications to the bare band, leveraging pumped and unpumped spectra to untangle the bare band from the modified band. The power of this technique is demonstrated best in Fig. 2e where the $\text{Im}\Sigma$ and $\text{Re}\Sigma$ used in the simulation that closely reproduces the MDC centroid locations are nearly identical to the measured $\text{Im}\Sigma$ and the $\text{Re}\Sigma$ derived from Kramers-Kronig.

Although our study focuses on slow electronic dynamics where a clear quasi-Fermi level can be established, our method for extracting the self-energy through spectral simulation (Supplementary Figs. 3 and 4) could be generalized to ultrafast dynamics where the adiabatic principle breaks down. For instance, the standard functional form of the self-energy for electron-phonon coupling can be replaced with a theoretical model for non-thermalized electrons since the procedure simply finds optimal parameters that minimize the MDC centroid differences, providing a method to test such models on real data, peering beneath the time-bandwidth product of ultrafast pulses.

Previous studies have demonstrated a large degree of variability in the measured EPC at the TSS^{20,27,33,34}. However, it has been shown that λ of the TSS is dependent on the bulk doping and presence of surface QW states^{25,34,35}. This study helps to untangle the complicated relationship between EPC and the bulk conduction band by demonstrating the sensitivity of λ on the DOS at the Fermi level of the quantized bulk bands. This sensitivity is seen in Fig. 2f where the EPC constant increase dramatically as the QW2 singularity passes the Fermi level. It is possible

that the variable electron-phonon coupling seen in previous reports is related to the variable dopings and variable degree of quantization in those samples and the consequential acute responsiveness of the EPC to the DOS at E_F .

Conclusion

We have demonstrated an ultrafast control of electron-phonon interaction via a photo-induced Lifshitz transition toggling a van-Hove-like singularity below the Fermi level. The subsequent relaxation of the quantum well spectrum reverses the Lifshitz transition at τ_{cross} triggering a large transient enhancement of the EPC, exceeding previously reported equilibrium values. The rapid transition of the QW2 DOS across the Fermi level accelerates direct phonon emission of the A_{1g}^2 optical phonon mode, thereby enabling rapid recombination of photogenerated surface electrons with spatially separated photogenerated holes in the bulk via c -axis scattering. As QW2 continues to drift upward in energy, phonon-mediated recombination freezes out due to a phonon-bottleneck process. Moreover, the electron-phonon scattering momentarily passes charge from the QWs to the TSS, producing an ultrafast modification to the QW energy levels at τ_{cross} . All together, this work establishes a simple means of controlling large changes in the DOS at the Fermi level and enhancement of electron-boson interactions on ultrafast timescales.

Methods

Sample preparation. The Bi_2Se_3 single crystals were grown by directional slow solidification and rendered p-type with ≈ 1 at. % Mg substitution with Bi. The crystals were cleaved and measured in vacuum at 5×10^{-11} Torr and at 80 K with LN_2 cooling. The sample underwent rapid dosing when it was initially exposed to the infrared pump. This led to the creation of a clear QW spectrum, which is similar to what Lin et al. observed¹⁷. There was no additional dosing that occurred after subsequent pumping. This dosing effect might be due to the presence of trapped gasses in either the graphite spray or the crystal itself. The results of this dosing were comparable to the effects of carbon monoxide and water surface dosing^{50,51}. We have observed this dosing effect multiple times, but only when using graphite spray on specifically p-type Bi_2Se_3 samples. For instance, we have extensively measured n-doped conductive samples and have not observed such a pump-induced dramatic dosing behavior. It is possible that a combination of the downward band-bending potential and ionization of gas species by the pump or probe beam enhances surface adsorption in the event of outgassing.

TR-ARPES details. The pump beam consists of 1.48 eV p-polarized photons generated in a cavity-dumped Ti:sapphire oscillator with repetition rates of 678.75 kHz - 1357.50 kHz. The probe beam consists of 5.94 eV p-polarized photons created through frequency quadrupling of the pump beam in two BBO stages. The pump and probe beam spot sizes are characterized by FWHMs of 120 μm and 30 μm , respectively. The energy and momentum resolution of the TR-ARPES system is ~ 25 meV and $\pm 0.003 \text{ \AA}^{-1}$, respectively⁵². The time resolution determined by the convolution of the pump and probe beams at pump-probe overlap is ~ 300 femtoseconds. The fluence dependence measurements were enabled by a variable neutral density filter on the pump beam, which had no measurable effect on the time resolution or beam size. All reported fluence values in this study refer to incident fluence on the Bi_2Se_3 surface. Single fluence analysis (see Figs. 2 and 3) are for $51.8 \mu\text{J} \cdot \text{cm}^{-2}$. All analysis was performed using PyARPES, an open-source analytical library tailored to ARPES measurements⁵³.

Data availability

All data used for analysis is made available upon request to the corresponding author.

Code availability

All code used for analyzing the data is made available upon request to the corresponding author.

Received: 31 October 2022; Accepted: 18 May 2023;

Published online: 26 June 2023

References

- Bardeen, J., Cooper, L. N. & Schrieffer, J. R. Theory of superconductivity. *Phys. Rev.* **108**, 1175–1204 (1957).
- Marsiglio, F. & Carbotte, J. P. *Electron-Phonon Superconductivity*, 73-162 (Springer Berlin Heidelberg, Berlin, Heidelberg, 2008).
- Grimvall, G. The electron-phonon interaction in normal metals. *Phys. Scripta* **14**, 63–78 (1976).
- Pouget, J.-P., Canadell, E. & Guster, B. Momentum-dependent electron-phonon coupling in charge density wave systems. *Phys. Rev. B* **103**, 115135 (2021).
- Lu, J. M. et al. Evidence for two-dimensional Ising superconductivity in gated MoS_2 . *Science* **350**, 1353–1357 (2015).
- Zhang, X.-L. & Liu, W.-M. Electron-phonon coupling and its implication for the superconducting topological insulators. *Sci. Rep.* **5**, 8964 (2015).
- van Heumen, E., Berben, M., Neubrand, L. & Huang, Y. Scattering rate collapse driven by a van Hove singularity in the dirac semimetal PdTe_2 . *Phys. Rev. Mater.* **3**, 114202 (2019).
- Lifshitz, I. Anomalies of electron characteristics of a metal in the high pressure region. *Soviet Phys. JETP* **11**, 1130–1135 (1960).
- Blanter, Y., Kaganov, M., Pantsulaya, A. & Varlamov, A. The theory of electronic topological transitions. *Phys. Rep.* **245**, 159–257 (1994).
- Markiewicz, R. A survey of the van Hove scenario for high- T_c superconductivity with special emphasis on pseudogaps and striped phases. *J. Phys. Chem. Solids* **58**, 1179–1310 (1997).
- Kim, K. et al. Importance of the van Hove singularity in superconducting PdTe_2 . *Phys. Rev. B* **97**, 165102 (2018).
- Zhang, Y. et al. Electronic evidence of temperature-induced Lifshitz transition and topological nature in zrte_5 . *Nat. Commun.* **8**, 15512 (2017).
- Mori, R. et al. Controlling a van Hove singularity and Fermi surface topology at a complex oxide heterostructure interface. *Nat. Commun.* **10**, 5534 (2019).
- Sen, S. & Guo, G.-Y. Pressure induced Lifshitz transition in ThFeAsN . *Phys. Rev. Mater.* **4**, 104802 (2020).
- Singh, G. et al. Gap suppression at a Lifshitz transition in a multi-condensate superconductor. *Nat. Mater.* **18**, 948–954 (2019).
- Ast, C. R. et al. Local detection of spin-orbit splitting by scanning tunneling spectroscopy. *Phys. Rev. B* **75**, 201401 (2007).
- Lin, C.-Y. et al. Orbital-dependent spin textures in Bi_2Se_3 quantum well states. *Phys. Rev. B* **98**, 075149 (2018).
- Ciocys, S. T., Maksimovic, N., Analytis, J. G. & Lanzara, A. Driving ultrafast spin and energy modulation in quantum well states via photo-induced electric fields. *npj Quant. Mater.* **7**, 79 (2022).
- Hayashi, H. et al. High-resolution angle-resolved photoemission study of electronic structure and electron self-energy in palladium. *Phys. Rev. B* **87**, 035140 (2013).
- Chen, C. et al. Tunable Dirac fermion dynamics in topological insulators. *Sci. Rep.* **3**, 2411 (2013).
- Ciocys, S., Morimoto, T., Moore, J. E. & Lanzara, A. Tracking surface photovoltage dipole geometry in Bi_2Se_3 with time-resolved photoemission. *J. Stat. Mech.* **2019**, 104008 (2019).
- Ciocys, S. et al. Manipulating long-lived topological surface photovoltage in bulk-insulating topological insulators Bi_2Se_3 and Bi_2Te_3 . *npj Quant. Mater.* **5**, 16 (2020).
- Ingle, N. J. C. et al. Quantitative analysis of Sr_2RuO_4 angle-resolved photoemission spectra: Many-body interactions in a model Fermi liquid. *Phys. Rev. B* **72**, 205114 (2005).
- Kondo, T. et al. Anomalous dressing of Dirac fermions in the topological surface state of Bi_2Se_3 , Bi_2Te_3 , and Cu-doped Bi_2Se_3 . *Phys. Rev. Lett.* **110**, 217601 (2013).
- Sobota, J. A. et al. Distinguishing bulk and surface electron-phonon coupling in the topological insulator Bi_2Se_3 using time-resolved photoemission spectroscopy. *Phys. Rev. Lett.* **113**, 157401 (2014).
- Cheng, W. & Ren, S.-F. Phonons of single quintuple Bi_2Te_3 and Bi_2Se_3 films and bulk materials. *Phys. Rev. B* **83**, 094301 (2011).
- Heid, R., Sklyadneva, I. Y. & Chulkov, E. V. Electron-phonon coupling in topological surface states: the role of polar optical modes. *Sci. Rep.* **7**, 1095 (2017).
- Irfan, B. et al. Temperature dependent Raman scattering studies of three dimensional topological insulators Bi_2Se_3 . *J. Appl. Phys.* **115**, 173506 (2014).
- Pan, Z.-H., Vescovo, E., Fedorov, A. V., Gu, G. D. & Valla, T. Persistent coherence and spin polarization of topological surface states on topological insulators. *Phys. Rev. B* **88**, 041101 (2013).
- Kordyuk, A. A. et al. Anomalously enhanced photoemission from the Dirac point and other peculiarities in the self-energy of the surface-state quasiparticles in Bi_2Se_3 . *Phys. Rev. B* **85**, 075414 (2012).
- Pan, Z.-H. et al. Measurement of an exceptionally weak electron-phonon coupling on the surface of the topological insulator Bi_2Se_3 using angle-resolved photoemission spectroscopy. *Phys. Rev. Lett.* **108**, 187001 (2012).

32. Fedorov, A. V. et al. Observation of a universal donor-dependent vibrational mode in graphene. *Nat. Commun.* **5**, 3257 (2014).
33. Lee, Y. J. et al. Weak surface electron-phonon coupling in the topological insulator Bi₂Se₃ nanoparticles revealed by electron spin resonance. *Appl. Phys. Lett.* **114**, 123101 (2019).
34. Benedek, G. et al. Origin of the electron-phonon interaction of topological semimetal surfaces measured with helium atom scattering. *J. Phys. Chem. Lett.* **11**, 1927–1933 (2020).
35. Ruckhofer, A. et al. Terahertz surface modes and electron-phonon coupling on Bi₂Se₃(111). *Phys. Rev. Res.* **2**, 023186 (2020).
36. Kralj, M. et al. Temperature dependence of photoemission from quantum-well states in Ag/V(100): Moving surface-vacuum barrier effects. *Phys. Rev. B* **64**, 085411 (2001).
37. Zhou, J. et al. Direct observation of large electron-phonon interaction effect on phonon heat transport. *Nat. Commun.* **11**, 6040 (2020).
38. Zhang, Z. & Yates, J. T. Band bending in semiconductors: chemical and physical consequences at surfaces and interfaces. *Chem. Rev.* **112**, 5520–5551 (2012).
39. Kung, H.-H. et al. Surface vibrational modes of the topological insulator bi₂se₃ observed by Raman spectroscopy. *Phys. Rev. B* **95**, 245406 (2017).
40. Liu, L., Zhang, M. & Liu, Q. The Raman spectra of Co-, Fe-, and Mn-doped Bi₂Se₃ single crystals. *Crystals* **13**, 456 (2023).
41. van Hest, J. J. H. A., Blab, G. A., Gerritsen, H. C., de Mello Donega, C. & Meijerink, A. The role of a phonon bottleneck in relaxation processes for Ln-doped NaYF₄ nanocrystals. *J. Phys. Chem. C* **122**, 3985–3993 (2018).
42. Wang, J. et al. Spin blockade and phonon bottleneck for hot electron relaxation observed in n-doped colloidal quantum dots. *Nat. Commun.* **12**, 550 (2021).
43. Sohler, T. et al. Enhanced electron-phonon interaction in multivalley materials. *Phys. Rev. X* **9**, 031019 (2019).
44. Sohler, T., Gibertini, M. & Verstraete, M. J. Remote free-carrier screening to boost the mobility of Fröhlich-limited two-dimensional semiconductors. *Phys. Rev. Mater.* **5**, 024004 (2021).
45. Poncé, S., Margine, E., Verdi, C. & Giustino, F. EPW: Electron-phonon coupling, transport and superconducting properties using maximally localized Wannier functions. *Comput. Phys. Commun.* **209**, 116–133 (2016).
46. Aidersburger, M., Kirchner, F. O., Krausz, F. & Baum, P. Single-electron pulses for ultrafast diffraction. *Proc. Natl Acad. Sci.* **107**, 19714–19719 (2010).
47. Levy, G., Nettke, W., Ludbrook, B. M., Veenstra, C. N. & Damascelli, A. Deconstruction of resolution effects in angle-resolved photoemission. *Phys. Rev. B* **90**, 045150 (2014).
48. Kaminski, A. & Fretwell, H. M. On the extraction of the self-energy from angle-resolved photoemission spectroscopy. *N. J. Phys.* **7**, 98–98 (2005).
49. Kirkegaard, C., Kim, T. K. & Hofmann, P. Self-energy determination and electron-phonon coupling on Bi(110). *N. J. Phys.* **7**, 99–99 (2005).
50. Benia, H. M., Lin, C., Kern, K. & Ast, C. R. Reactive chemical doping of the Bi₂Se₃ topological insulator. *Phys. Rev. Lett.* **107**, 177602 (2011).
51. King, P. D. C. et al. Large tunable Rashba spin splitting of a two-dimensional electron gas in Bi₂Se₃. *Phys. Rev. Lett.* **107**, 096802 (2011).
52. Smallwood, C. L., Jozwiak, C., Zhang, W. & Lanzara, A. An ultrafast angle-resolved photoemission apparatus for measuring complex materials. *Rev. Sci. Instrum.* **83**, 123904 (2012).
53. Stansbury, C. & Lanzara, A. PyARPES: An analysis framework for multimodal angle-resolved photoemission spectroscopies. *SoftwareX* **11**, 100472 (2020).

Acknowledgements

This work was supported by the Director, Office of Science, Office of Basic Energy Sciences, Materials Sciences and Engineering Division, of the U.S. Department of Energy, under Contract No. DE-AC02-05CH11231, as part of the Ultrafast Materials Science Program (KC2203). A.L. also acknowledges support from the Gordon and Betty Moore Foundation EPIQS Initiative through Grant No. GBMF4859 for the implementation of the experimental setup.

Author contributions

S.C. performed the ARPES measurements and the analysis. A.L. and S.C. developed the experimental premise and infrastructure. Both authors contributed to writing the manuscript.

Competing interests

The authors declare no competing interests.

Additional information

Supplementary information The online version contains supplementary material available at <https://doi.org/10.1038/s43246-023-00370-7>.

Correspondence and requests for materials should be addressed to Alessandra Lanzara.

Peer review information *Communications Materials* thanks the anonymous reviewers for their contribution to the peer review of this work. Primary Handling Editors: Klaas-Jan Tielrooij and Aldo Isidori. A peer review file is available.

Reprints and permission information is available at <http://www.nature.com/reprints>

Publisher's note Springer Nature remains neutral with regard to jurisdictional claims in published maps and institutional affiliations.



Open Access This article is licensed under a Creative Commons Attribution 4.0 International License, which permits use, sharing, adaptation, distribution and reproduction in any medium or format, as long as you give appropriate credit to the original author(s) and the source, provide a link to the Creative Commons license, and indicate if changes were made. The images or other third party material in this article are included in the article's Creative Commons license, unless indicated otherwise in a credit line to the material. If material is not included in the article's Creative Commons license and your intended use is not permitted by statutory regulation or exceeds the permitted use, you will need to obtain permission directly from the copyright holder. To view a copy of this license, visit <http://creativecommons.org/licenses/by/4.0/>.

© The Author(s) 2023